Journal of Magnetic Resonance 206 (2010) 41–51

Contents lists available at ScienceDirect

Journal of Magnetic Resonance

journal homepage: www.elsevier.com/locate/jmr

Optimizing gradient waveforms for microstructure sensitivity in diffusion-weighted MR

Ivana Drobnjak [a,*], Bernard Siow [a,b], Daniel C. Alexander [a]

[a] Center for Medical Image Computing, Department of Computer Science, University College London (UCL), Gower Street, London WC1E 6BT, UK
[b] Centre for Advanced Biomedical Imaging (CABI), Department of Medicine and Institute of Child Health, University College London (UCL), London WC1E 6DD, UK

ARTICLE INFO

Article history:
Received 29 March 2010
Revised 24 May 2010
Available online 1 June 2010

Keywords:
Axon diameter
Microstructure
Generalized gradient waveform
Diffusion MR
Oscillating gradients
Pore size
PGSE
OGSE

ABSTRACT

Variations in gradient waveforms can provide different levels of sensitivity to microstructure parameters in diffusion-weighted MR. We present a method that identifies gradient waveforms with maximal sensitivity to parameters of a model relating microstructural features to diffusion MR signals. The method optimizes the shape of the gradient waveform, constrained by hardware limits and fixed orientation, to minimize the expected variance of parameter estimates. The waveform is defined discretely and each point optimized independently. The method is illustrated with a biomedical application in which we maximize the sensitivity to microstructural features of white matter such as axon radius, intra-cellular volume fraction and diffusion constants. Simulation experiments find that optimization of the shape of the gradient waveform improves sensitivity to model parameters for both human and animal MR systems. In particular, the optimized waveforms make axon radii smaller than 5 μm more distinguishable than standard pulsed gradient spin-echo (PGSE). The identified class of optimized gradient waveforms have dominant square-wave components with frequency that increases as the radius size decreases.

1. Introduction

Diffusion-weighted MR is a non-destructive probe into the microstructure of materials, and can provide insight into pore morphology and fluid transport [1]. The technique is therefore useful for studying porous structures such as sandstone rocks, catalysts, colloids and biological tissues and is used for example in paint and drilling industry [2], food industry [3–6], studying minerals [7] or biomedical sciences [8–11].

The application that motivates this work is biomedical imaging where diffusion MRI offers the potential to map microstructural features in tissue. For example, in nervous tissue such as white matter in the brain, axon radius affects nerve function as it determines the conduction velocity [12,13], which controls the delay between the receipt of a stimulus by a nerve and the response to it. Thus imaging axon radius is a key challenge [8–10] as a reliable technique could provide insight into neuronal diseases that alter axon radius distribution, such as autism [14,15], amyotrophic lateral sclerosis (ALS) [16,17] or schizophrenia [18,19]. In addition, recent research suggests that aggressive tumors are usually characterized with a larger cell nuclear size [20]. Early studies to measure cell nuclear size with diffusion MRI [11] and use it for diagnostic purposes in cancers show promise.

The simplest and most commonly used pulse sequence in diffusion MRI is the pulsed gradient spin-echo sequence (PGSE). The standard PGSE sequence has a pair of equal approximately rectangular (constant over an interval and zero outside) gradient pulses either side of the refocussing pulse in a spin-echo sequence. Techniques for estimation of microstructure parameters that use the standard PGSE sequence rely on strong gradient strengths and long acquisition times [8–10,21–26], which makes them impractical for human in vivo studies since human imaging systems have limited gradient strengths of up to around 0.08 T/m. Sensitivity to pore size depends critically on gradient strength and the ability to distinguish small radii decreases rapidly as gradient strength decreases. Alexander [21] demonstrates in simulation that, by carefully choosing the combination of PGSE settings, a human scanner with 0.07 T/m gradients can estimate axon radii down to about 2.5 μm reliably while smaller radii are identifiable as small but indistinguishable from one another. Later work [27] shows promising results in fixed tissue and the brain. Barazany et al.'s [10] results suggest that axon diameters down to 0.2 μm are distinguishable in an in vivo rat experiment, with 0.3 T/m gradients. Barazany assumes known fiber orientation whereas Alexander et al. [21,27] do not, thus the lower limit for human scanners may decrease slightly if orientation is known.

Alternative gradient waveforms potentially discriminate smaller pore sizes. Oscillating gradient spin-echo (OGSE) sequences have similar basic structure to standard PGSE, but use sinusoid

* Corresponding author.
E-mail address: i.drobnjak@cs.ucl.ac.uk (I. Drobnjak).

1090-7807/$ - see front matter © 2010 Elsevier Inc. All rights reserved.
doi:10.1016/j.jmr.2010.05.017

waveforms instead of the rectangular pulses. These sequences measure the diffusion behavior on the time scale of the period of each oscillation, hence higher frequency of the oscillating gradients corresponds to a smaller effective diffusion time, which helps distinguish smaller pore sizes [28,11,29,30]. Other waveforms, such as chirped [31], that contain a range of frequencies may provide even greater sensitivity.

Here we use a stochastic optimization procedure to search for a combination of gradient waveforms that are most sensitive to microstructure parameters typical in biomedical applications. We use the same basic pulse sequence structure as the PGSE and the OGSE sequence, but replace the rectangular or the sinusoidal pulses, with waveform defined discretely by a sequence of values that are free to vary independently. We optimize an imaging protocol consisting of several measurements, each with their own waveform, to maximize their sensitivity to the parameters of a simple model that includes the axon radius.

We build on the optimization framework in [21], which optimizes a protocol consisting only of rectangular PGSE measurements for sensitivity to the model parameters. The optimization in [21] seeks the pulse sequence parameters (gradient strength G, diffusion time Δ and gradient duration δ) that minimize the mean Cramer-Rao Lower Bound (CRLB) of the parameters. To extend the framework for generalized gradient waveforms, constrained only by hardware limits and fixed orientation, we use the matrix formalism to calculate the diffusion signal [32,33], and optimize each point on each waveform. Experiments demonstrate the new optimization using the same simplified version of the CHARMED model [34] which was used in [21]. Further, they compare the sensitivity of the optimized generalized waveform protocols to rectangular PGSE protocols and study, in simulation, the ability of both optimized protocols to recover axon radius.

We start with the outline of the tissue and signal model together with the optimization framework in Section 2. Experiments follow which compare sensitivity to model parameters, over a range of axon radii, of optimized generalized waveform protocols and optimized rectangular waveform protocols in Section 3. Finally, Section 4 summarises findings, highlights limitations, and suggests further work and applications.

2. Methods

This section first describes the model used to calculate the diffusion MR signal. It then describes the optimization framework used to determine the shape of the gradient waveform.

2.1. Tissue model

The white matter tissue model which we use is described in [21]. It is a two compartment model similar to Assaf et al.'s composite hindered and restricted model of diffusion (CHARMED) [34], but with a single axon radius rather than a distribution and assuming cylindrical symmetry of the apparent diffusion tensor in the extra-cellular space. The model assumes parallel non-abutting cylindrical axon cells of fixed direction, with equal radii and impermeable walls embedded in a homogenous extra-cellular medium. The parameters of the model are: the volume fraction $f \in [0,1]$ of the intra-cellular compartment; the axon direction $\mathbf{n}$; the axon radius a; the restricted diffusion coefficient D_r; and the hindered diffusion coefficient D_h. Ref. [21] gives a more complete description of the tissue model.

2.2. Pulse sequence model

The pulse sequence model has the same basic structure as the PGSE sequence, with two generalized (arbitrary) gradient waveforms in place of the two fixed rectangular pulses as Fig. 1 illustrates.

The rectangular pulses are identical, and placed one on each side of the 180° RF pulse, first one starting T_{prep} time after the 90° RF pulse is finished. They are defined with three parameters: the maximal gradient strength G; the length of the gradient pulses δ; and the time between the onsets of the two pulses Δ.

The generalised gradient waveforms, g_o, are placed one on each side of the 180° RF pulse. The first one, $g_o(n\tau)$, $n = 1,\ldots,N$, is parametrized with N equally spaced points, and starts T_{prep} time after the 90° RF pulse is finished. The second one is the mirror reflection of the first. The full representation of the gradient in time is

$$g(n\tau) = \begin{cases} 0 & 0 \leqslant n < N_1 \\ g_o((n - N_1 + 1)\tau) & N_1 \leqslant n < N_1 + N \\ 0 & N_1 + N \leqslant n < N_1 + N + N_2 \\ g_o((N_1 + 2N + N_2 - n)\tau) & N_1 + N + N_2 \leqslant n < N_1 + 2N + N_2 \\ 0 & N_1 + 2N + N_2 \leqslant n, \end{cases} \quad (1)$$

where $N_1 = integ((\mathrm{P90}/2 + T_{prep})/\tau)$ is the number of steps before the gradient starts,[1] $N_2 = integ(\mathrm{P180}/\tau)$ is the number of steps during the 180° RF pulse and $N = integ((\mathrm{TE}/2 - \mathrm{P180}/2 - \mathrm{P90}/2 - T_{prep})/\tau)$ is the number of steps during one gradient waveform, n is an integer, TE is the echo time, P90 and P180 are respective durations of the 90° and 180° RF pulses, and τ is a fixed time interval.

We refer to the generalized waveforms as *gen* and to the rectangular waveforms as *rec* throughout the rest of this paper. Fig. 1 illustrates the schematic representation of both *gen* and *rec* pulse sequences. We assume that the gradient direction for both sequences is fixed and perpendicular to the fiber direction.

2.3. Signal model

Following [34], we write the diffusion MR signal

$$E = fE_r + (1 - f)E_h, \quad (2)$$

where E_r and E_h are normalized MR signals coming from the restricted (intra-cellular) and the hindered (extra-cellular) compartments respectively. The hindered diffusion produces Gaussian displacement distribution so that [35,36]:

$$E_h = \exp\left(-\gamma^2 D_h \int_0^{\mathrm{TE}} [F(t) - 2H(t - \mathrm{TE}/2)F(\mathrm{TE}/2)]^2 \mathrm{d}t\right), \quad (3)$$

where

$$F(t) = \int_0^t g(t')\mathrm{d}t', \quad (4)$$

$H(t)$ is the Heaviside step function and γ is the gyro-magnetic ratio.

To estimate the diffusion signal from the restricted compartment E_r, we use the matrix formalism developed by Callaghan [32,33],[2] which can be used for both weak and strong diffusion gradients. To use the matrix method, we quantize the gradient amplitude $g_o(n\tau)$ into steps of size g_{step}. This way, at time $n\tau$ the amplitude is $m_n q$ where $q = (2\pi)^{-1}\gamma\tau g_{step}$, and m_n is given by

$$m_n = integ(g_o(n\tau)/g_{step}), \quad (5)$$

As shown in [32], we use the eigenmode expansion to describe the diffusion propagator

[1] *integ* rounds to the nearest integer.

[2] We made some minor adaptations to the method in [33], in order to improve the implementation (contact the authors for details) and agreement with models in simple geometries.

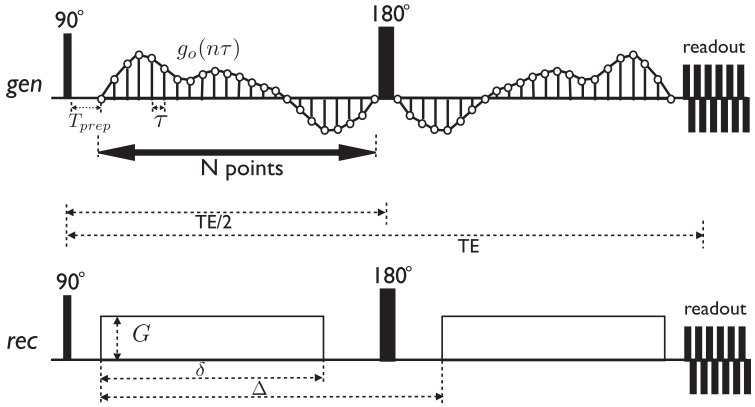

Fig. 1. Schematic representation of the PGSE sequence with generalized gradient waveforms *gen* (top) vs. the standard PGSE with rectangular gradient waveforms *rec* (bottom). The generalized gradient waveforms are mirrored about the 180° RF pulse, and amplitudes $g_o(n\tau)$, $n = 1,\ldots,N$ are optimized to give any shape. Points on the waveforms are separated with equal time intervals τ. The rectangular waveforms have fixed shape and are optimized by tuning G, δ and Δ.

$$P(\mathbf{r}|\mathbf{r}',t) = \sum_{n=0}^{\infty} \exp(-\lambda_n t) u_n(\mathbf{r}) u_n^*(\mathbf{r}'), \tag{6}$$

which gives the probability that a spin starting at position $\mathbf{r}$ will move to $\mathbf{r}'$ at a later time t, and where $u_n(\mathbf{r})$ are an orthonormal set of solutions to the Helmholtz equation parametrized with corresponding eigenvalues λ_n. The signal attenuation can then be written as a matrix product

$$E_r = S(\mathbf{q})R[A(\mathbf{q})]^{m_2}\cdots R[A(\mathbf{q})]^{m_N}R^L[A(\mathbf{q})]^{m_N}R\cdots[A(\mathbf{q})]^{m_2}RS^*(-\mathbf{q}) \tag{7}$$

where the elements of the matrices S, A and R are

$$S_n(\mathbf{q}) = V^{-1/2}\int u_n(\mathbf{r})\exp(i2\pi\mathbf{q}\cdot\mathbf{r})d\mathbf{r} \tag{8}$$

$$R_{nn} = \exp(-\lambda_n\tau) \tag{9}$$

$$A_{nn'}(\mathbf{q}) = \int u_n^*(\mathbf{r})u_{n'}(\mathbf{r})\exp(i2\pi\mathbf{q}\cdot\mathbf{r})d\mathbf{r}, \tag{10}$$

V is the pore volume, and $\mathbf{q} = q\mathbf{g}$ where $\mathbf{g}$ is the unit gradient vector. For the tissue model in Section 2.1 we assume cylindrical geometry and introduce cylindrical polar coordinates in which the longitudinal z-axis is a symmetry axis for the system. We fix the gradient direction along the x-axis. The relevant polar coordinates are (r,θ) where $r\in[0,a]$, $\theta\in[0,2\pi]$, and the eigenvectors become

$$u_n(r,\theta) = \alpha_{nk}J_n\left(\beta_{nk}\frac{r}{a}\right)\cos(n\theta), \tag{11}$$

where α_{nk} are the normalization constants

$$\alpha_{nk} = \sqrt{\frac{2\beta_{nk}^2}{\pi a^2 J_n^2(\beta_{nk})(\beta_{nk}^2 - n^2)}}, \quad n\neq 0 \tag{12}$$

$$\alpha_{0k} = \sqrt{\frac{\beta_{0k}^2}{\pi a^2 J_0^2(\beta_{0k})(\beta_{0k}^2)}}, \quad n = 0,$$

J_n are standard (cylindrical) Bessel functions of order n, and β_{nk} is the kth root of the equation $J_n'(\beta_{nk}) = 0$ [32,33]. The eigenvalues are

$$\lambda_n = \frac{\beta_{nk}^2 D_r}{a^2}. \tag{13}$$

We include terms in the eigenmode expansion (Eq. (6)) only from the largest twenty β_{nk} which provides sufficient accuracy [32].

2.4. The optimization framework

This section sets out the framework for optimizing the imaging protocol. The protocol consists of M measurements each with a different discretized gradient waveform. We seek the $m_{ij}, i = 1,\ldots,M$, $j = 1,\ldots,N$ that maximize sensitivity to the model parameters.

The objective function

$$F = \sum_{i=1}^{W}(J^{-1})_{ii}/w_i^2 \tag{14}$$

reflects the precision of the model parameter estimates, and is defined as the sum of normalized CRLBs, for the model parameters ω_i, $i = 1,\ldots,W$, where $(J^{-1})_{ii}$ is the CRLB for ω_i. Here, $W = 4$ and the ω_i are f, D_r, D_h and a. The CRLB provides a lower bound on the variance of a fitted model parameter that often correlates closely with the true variance. We assume a Rician noise model; the full expression for the CRLB assuming the Rician noise is in [21].

Optimization of the discretized waveform amplitudes tunes the m_{ij}, while the time and the gradient strength units τ and g_{step} are both fixed. Thus we need to calculate the unit q value and matrices A, S and R only once prior to optimization. We calculate these using standard MATLAB functions. To ensure feasibility of the sequence on standard scanners, the optimization enforces gradient hardware constraints onto the discretized waveform amplitudes m_{ij}: maximum gradient strength $0 \leqslant |m_{ij}g_{step}| \leqslant |G_{max}|$, and the maximum slew rate $0 \leqslant |(m_{ij} - m_{ij-1})g_{step}|/\tau \leqslant S_R$, where S_R is the slew rate. We enforce the maximum slew rate by setting the time interval $\tau > 2|G_{max}|/S_R$.

We use a stochastic optimization algorithm, self-organizing migratory algorithm (SOMA) [37] with population size of 50, 500 migrations and otherwise default settings, to perform the minimization. The full optimization runs SOMA five times and picks the result with the smallest final value of the objective function. The SOMA algorithm is parallelized using MATLAB distributed toolbox, and a standard run takes 5 h on 16 processors.

The algorithm above optimizes the protocol for a fixed TE, which is the same for all the measurements. However, the choice of TE affects the sensitivity to the model parameters significantly, because longer TE allows longer and more complex waveforms but also reduces signal through T_2 decay. Here we optimize the choice of TE crudely by running the optimization separately at several TEs and taking the one that minimizes F. The noise level used to calculate the objective function is adjusted in line with the optimized TE, as in [21].

3. Experiments and results

This section shows the results of three experiments. The first compares optimized generalized waveform protocols for different

hardware limits. The second and third experiments evaluate optimized generalized waveform protocols against the optimized rectangular waveform (standard PGSE) protocols. The second compares the sensitivity to model parameters by comparing the value of their respective objective functions. The third compares the ability to recover model parameters by comparing their respective posterior distributions.

3.1. Experiment 1: Optimized generalized gradient waveforms

The experiment tests three settings of gradient system. The first one, $G_{max} = 0.04$ T/m, slew rate $S_R = 200$ T/m/s, is typical of current human systems. The second one, $G_{max} = 0.08$ T/m, $S_R = 400$ T/m/s, is at the limit of what modern human scanners can achieve on live subjects. The third one, $G_{max} = 0.4$ T/m, $S_R = 2000$ T/m/s, is achievable in modern small-bore animal scanners. We assume δ-function priors on the model parameters: $f = 0.7, D_r = 1.7 \times 10^{-9}$ m^2/s and $D_h = 1.2 \times 10^{-9}$ m^2/s. We assume multiple δ-function priors on axon radius $a \in \{0.5, 1, 2, 3, 5\}$ μm, and optimize the protocol separately for each. The protocol consists of $M = 4$ measurements following [21].

We optimize separately for each TE $\in \{0.04, 0.06, 0.08, 0.1, 0.12\}$ s. We set the SNR of the unweighted (no gradients) signal at 20 when TE = 0.08 s and use $T_2 = 0.07$ s, which is typical for white matter, to adjust for different TE. Duration of the RF pulses and preparation time are as in [21]: P180 = 0.005s, P90 = 0.0025 s, $T_{prep} = 0.0059$ s. The waveform unit-parameters $\tau = 0.00041$ s and $g_{step} = 0.0004$ T/m are a couple of orders of magnitude smaller than the diffusion times and maximum gradient strength to ensure that the discrete waveform function is a good approximation of the continuous waveform. The time interval τ also satisfies $\tau \ll a^2/D_r$, making sure that the narrow pulse approximation is valid within each time interval.

Figs. 2–4 show the optimized generalized gradient waveforms, $g_o(n\tau), n = 1, \ldots, N$ for the human scanner values $G_{max} = 0.04$ T/m and $G_{max} = 0.08$ T/m, and animal scanner value $G_{max} = 0.4$ T/m respectively. Each row corresponds to a different radius a, and shows the four optimized measurements for that a.

We consistently observe a square-wave pattern emerge in the optimized waveforms and each protocol contains square-wave gradient waveforms with a range of frequencies. Broadly, however, the frequency of the square waves increases as radius decreases. The amplitude of the square-waves is consistently equal to G_{max}. These observations are consistent for all three gradient systems.

The duration of the waveforms vary for different radii because of differences in the optimized TEs. Table 1 shows the TE values that minimize F for each gradient system and each radius. For radii larger than 3 μm, the TE value decreases with increasing maximum gradient strength which reflects the fact that higher gradients allow similar sensitization in a shorter time. However, for radii smaller than 2 μm, the TE value remains similar over all gradient strengths, which suggest that longer pulses are required to get optimal sensitivity and the optimization finds the largest pulse duration with acceptable T_2 decay. The anomalous low TE for $a = 0.5$ μm and $G_{max} = 0.04$ T/m likely reflects the lack of any sensitivity to low a at this low gradient strength; lower TE increases signal and thus sensitivity to the other parameters.

3.2. Experiment 2: Comparison of the objective functions

This experiment evaluates the optimized generalized waveform protocol against the optimized rectangular waveform protocol by comparing the value of their respective objective functions. To

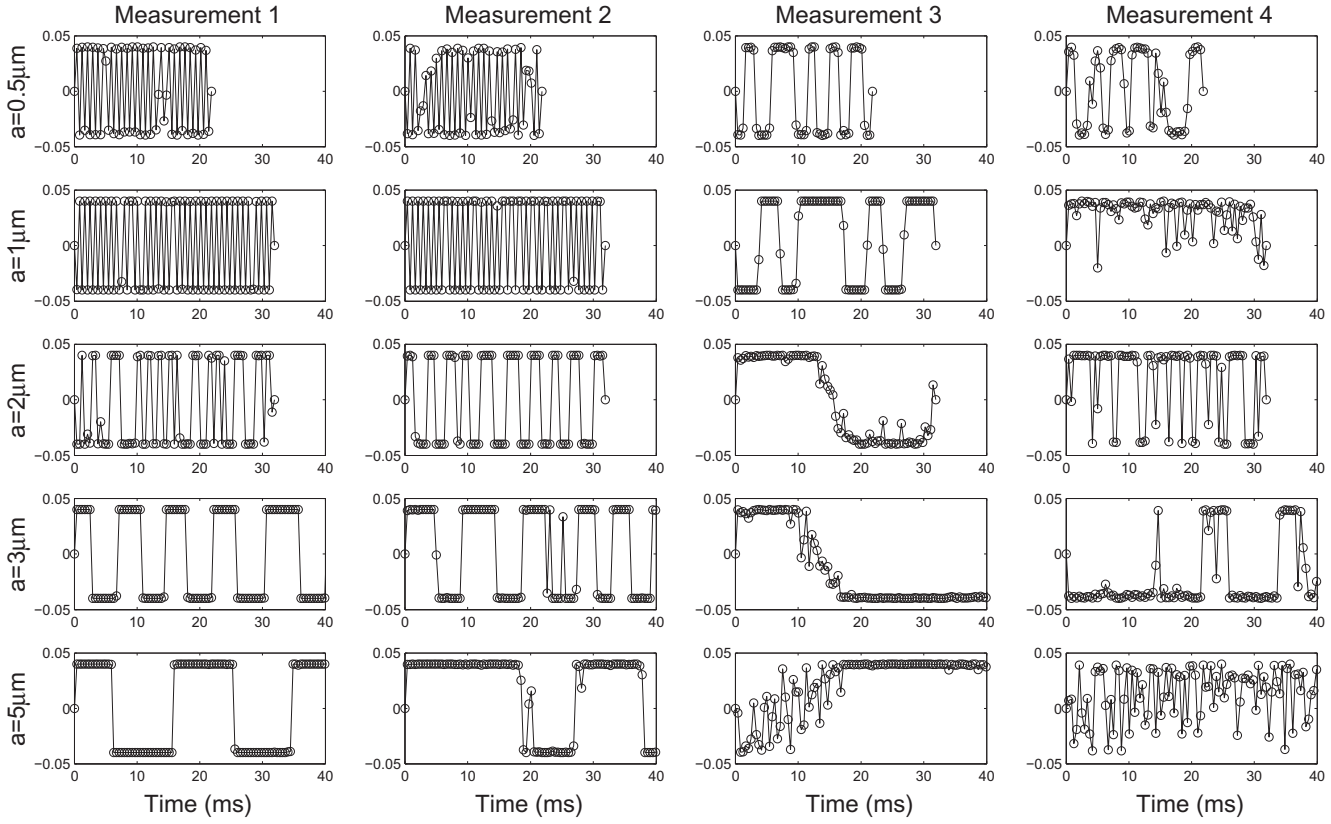

Fig. 2. Optimized generalized gradient waveforms $g_o(n\tau)$, $n = 1, \ldots, N$ when $G_{max} = 0.04$ T/m. There are four measurements for each a-priori setting of radius a. The measurements are ordered with decreasing dominant frequency of oscillations, with the measurements of the highest dominant frequency in the first column from the left.

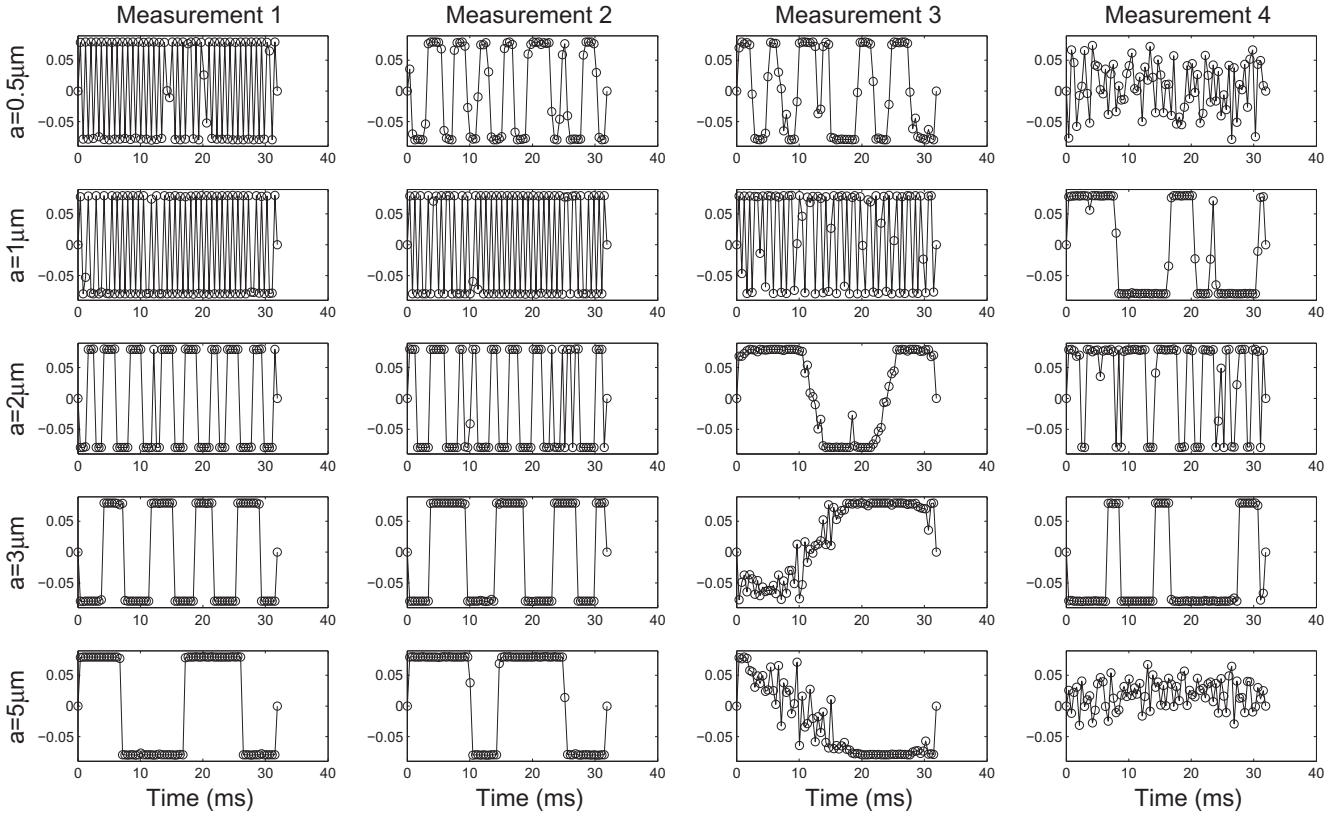

Fig. 3. As Fig. 2 for G_{max} = 0.08 T/m.

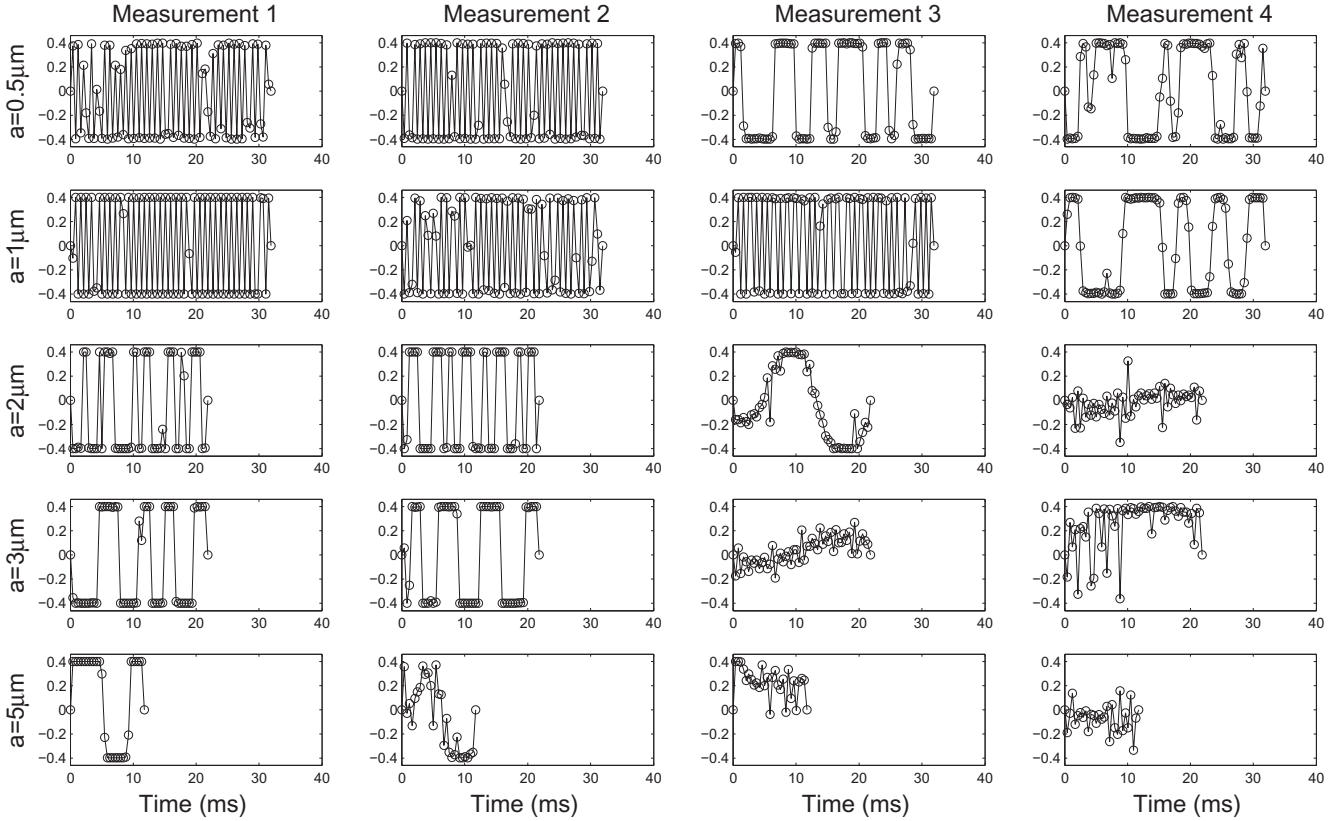

Fig. 4. As Fig. 2 for G_{max} = 0.4 T/m.

Table 1
Optimized TE values (in ms).

a (μm)	0.5	1	2	3	5
G_{max} = 0.04 T/m, S_R = 200 T/m/s	80	100	100	120	120
G_{max} = 0.08 T/m, S_R = 400 T/m/s	100	100	100	100	100
G_{max} = 0.4 T/m, S_R = 2000 T/m/s	100	100	80	80	60

optimize the rectangular waveform sequence we search the set of combinations of G, δ and Δ to minimize the objective function F as described in [21]. We use the same model and parameter values as for the generalized waveform optimization.

Fig. 5 shows the value of the objective function as a function of radius a for all different gradient settings. We consistently obtain lower values of the objective function for *gen* compared to *rec*,

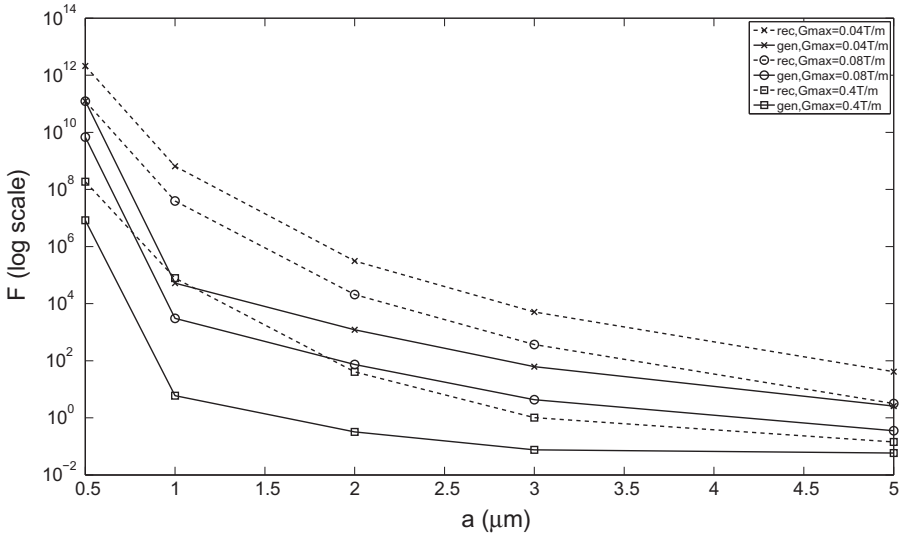

Fig. 5. Comparison of the objective function values of optimized generalized and rectangular (standard PGSE) waveform sequences.

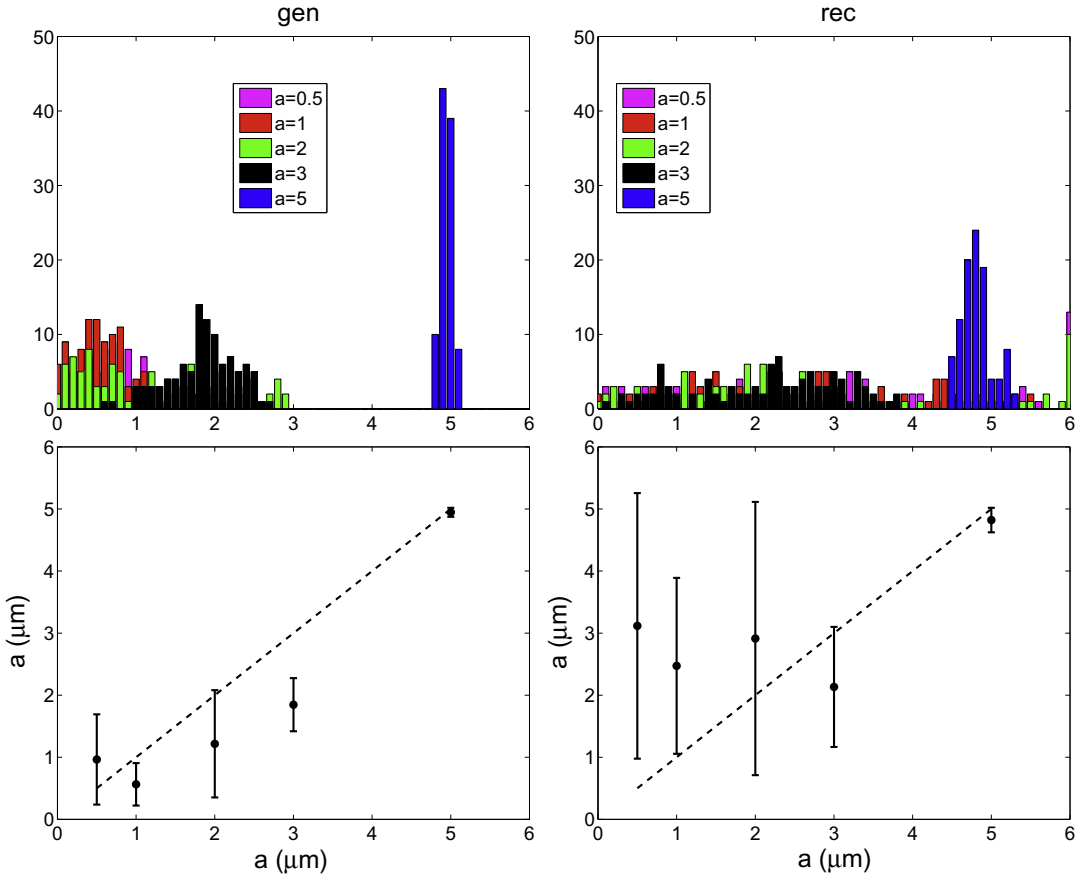

Fig. 6. G_{max} = 0.04 T/m. *Top row:* Posterior distributions on radius a (in μm) for the generalized waveform and the rectangular waveform (standard PGSE) sequence. *Bottom row:* Mean and standard deviations of posterior distributions. The true values of the radii are on the diagonal.

which suggests greater sensitivity to the model parameters. The strength of the gradients (G_{max}) also reduces the objective function confirming that the sensitivity increases for larger gradient strengths.

3.3. Experiment 3: Comparing the estimated model parameters

This experiment evaluates the optimized generalized waveform sequence against the optimized rectangular waveform sequence by comparing the precision and accuracy of the estimated model parameters. The simple MCMC procedure in [21] provides samples of the posterior distributions of the model parameters given the data. We generate synthetic data for both *gen* and *rec* waveforms using the optimized protocols in Experiments 1 and 2. We add Rician noise to each measurement so that for the unweighted (no gradients) image SNR = 20 [21]. To fit the model, we assume 250 repeats of each of the four measurements with independent noise. We initialized the model parameters to their true value to speed up convergence.

Figs. 6–8 show the posterior distributions on radius a for G_{max} = 0.04, 0.08 and 0.4 T/m respectively. The posterior distributions are markedly narrower for the optimized generalized waveforms, demonstrating higher precision in estimating the radius than the optimized rectangular waveforms. The bottom rows of the figures confirm that the generalized gradients sequence produce more accurate (closer to the diagonal) and precise (smaller error bars) estimates compared to the rectangular gradients sequence. The posterior distributions are also narrower for the stronger gradient strength for both type of waveforms.

Figs. 9–11 show the mean and standard deviation of posterior distributions on model parameters f, D_r and D_h for G_{max} = 0.04, 0.08 and 0.4 T/m respectively. With *gen*, the mean of the posterior distributions are closer to their true value, and standard deviation bars are smaller for all three model parameters, than with *rec* over all radius sizes. As for the axon radius, the estimates are closer to the true values as the gradient strength increases.

4. Discussion

Here we demonstrated the optimization framework for the estimation of the axon radii. Optimizing the shape of the gradient waveforms produces results which suggest greater sensitivity to microstructure parameters than conventional rectangular gradient waveforms. The optimization of the shape of the waveform makes the objective function consistently lower for all axon radius sizes, as seen in Fig. 5. Furthermore, the generalized waveform results demonstrate higher precision and accuracy of axon radius estimates than the optimized rectangular waveforms (as seen in Figs. 6–8) over all maximum gradient strengths G_{max}. The same is true for all the other model parameter estimates.

Square wave oscillations appear consistently in the optimized protocols. The frequency of the waveforms increases as the radius size decreases. These findings support previous work [11,28,29] that models the signal from sinusoid oscillating gradient pulses and shows that higher frequency corresponds to a smaller effective diffusion time, which provides sensitivity to smaller pore sizes. Each period of the oscillation is similar to a separate standard PGSE experiment with two single rectangular pulses and with diffusion time similar to the time period of the oscillation; multiple periods emphasise sensitivity to displacements over that diffusion time. One new and interesting feature of our optimized waveforms, is that we get square, and not sinusoidal, waves most likely because

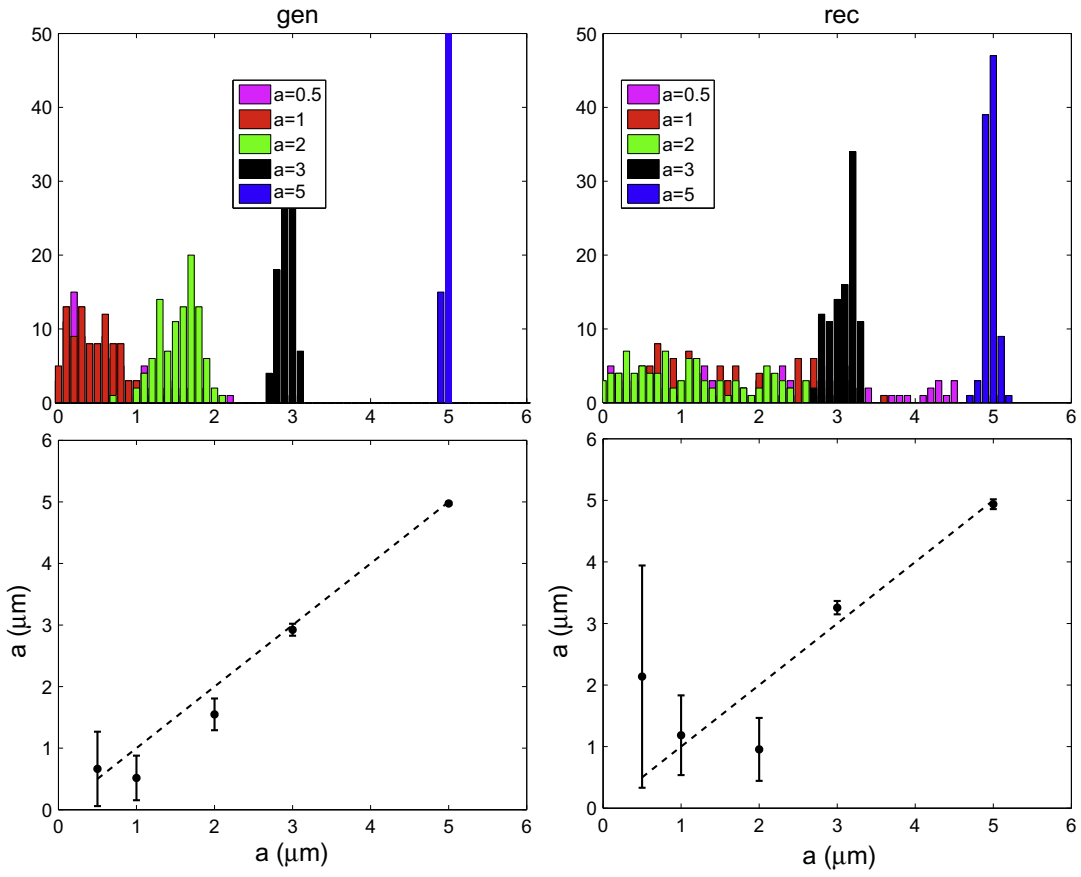

Fig. 7. As Fig. 6 for G_{max} = 0.08 T/m.

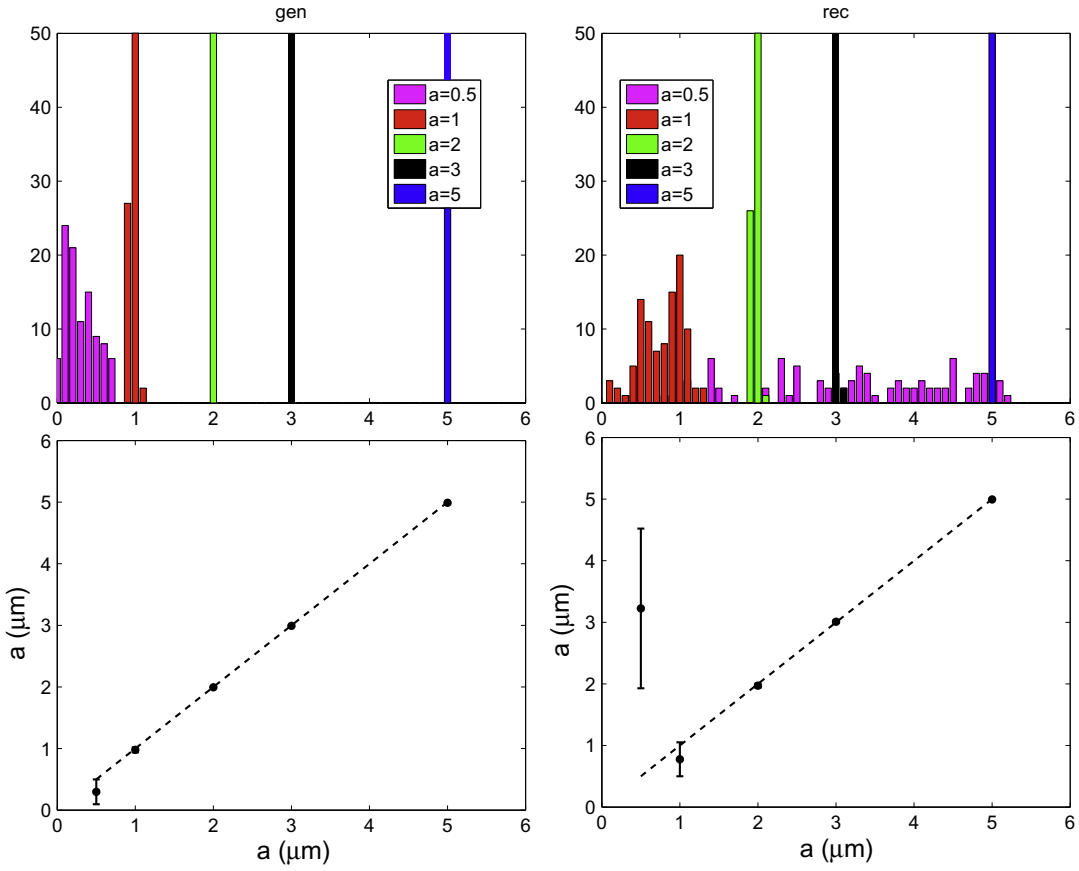

Fig. 8. As Fig. 6 for G_{max} = 0.4 T/m.

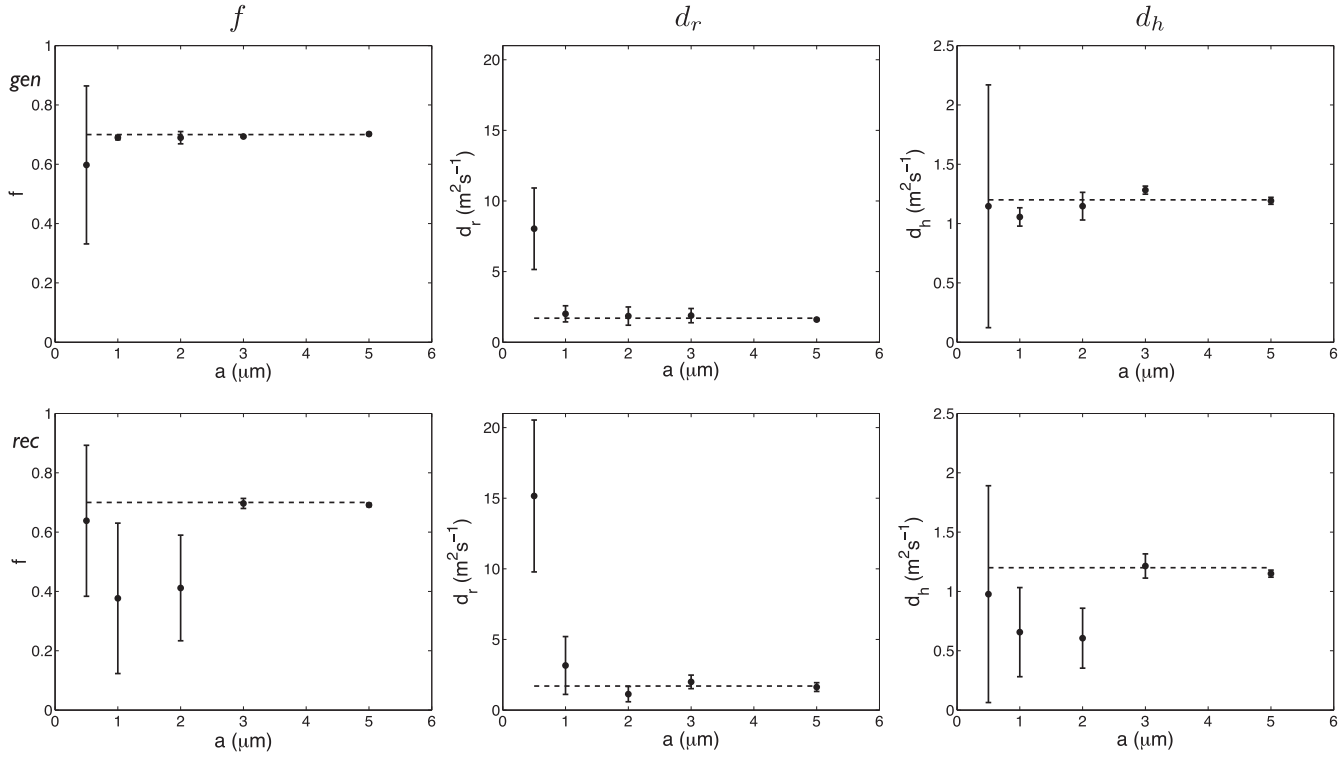

Fig. 9. G_{max} = 0.04 T/m. Mean and standard deviations of posterior distributions on model parameters f, D_r, D_h for the generalized waveform (*gen*) and the rectangular waveform (*rec*) sequence. The true values of the parameters are shown with dashed lines.

the square-wave maximizes the diffusion weighting in each period of the waveform.

Higher gradient strength increases the ability to distinguish smaller axon radii. It also gives much more accurate and precise estimates of all model parameters. The differences are quite dramatic, for both generalized and rectangular waveforms. Higher gradient strength provides greater diffusion weighting over shorter diffusion times which helps distinguish smaller radii. Another advantage of higher gradient strength is to allow acquisitions with shorter TE, and hence higher SNR.

The high dimensionality of the search space makes the global optimum set of waveforms hard to find. Although the waveforms we find approximate square-waves, most contain glitches and departures and some appear almost random noise. Increasing the population size in the algorithm makes only slight improvements, most likely because the apparently noisy features in the waveforms decrease sensitivity only very slightly compared to the perfect waves we might expect at the global optimum. We view this general waveform optimization as a tool for identifying the class of waveform most sensitive to a particular system rather than the exact solution. Once we have identified the class of waveforms, we can reduce dimensionality to improve convergence using more targeted optimizations. With the model we use here, for example, we might constrain each measurement of the protocol to have square-wave pulses and optimize just the amplitude, frequency and duration of each.

Furthermore, the optimization suggests that the highest frequency waveform is the same for 0.5 μm and 1 μm radius. However the high frequency waveform in both protocols reach the maximum possible with the fixed time interval τ. A limitation of the current implementation is that it cannot represent higher frequency oscillation that are still achievable if the amplitude is lower. This may explain the dramatic reduction in accuracy of parameter estimates when radius $a = 0.5$ μm compared to higher settings of a (see Figs. 9, 10). We could adapt the waveform representation to accommodate this, but the numerical implementation of reducing the constraints on τ is complex. Since, as mentioned above, this very general optimization is primarily meant to identify the broad class of protocols the added complexity seems unnecessary.

Here we limit the technique to optimize sequences with the same structure as the standard PGSE sequence, but other pulse sequences can provide diffusion MR measurements that may be better for estimating the parameters of particular models. For example, the multi-PGSE sequence involves multiple consecutive PGSE blocks. Each PGSE block, comprising a pair of gradients of duration δ, sensitizes the signal to motion that occurs during an interval Δ [38]. A previous study [38] suggests that multi-PGSE sequence make it possible to measure smaller pore sizes, to improve the accuracy of pore size measurements and potentially to distinguish different pore shapes. In particular, a special case of multi-PGSE sequences with two PGSE blocks, double-PGSE, have received increasing attention recently because such experiments are sensitive to restricted diffusion even for diffusion times that are long compared to the pore dimensions [39]. STEAM [40] and steady-state free procession (SSFP) [41] allow measurements with much longer diffusion times by avoiding T2 decay outside the gradient pulses. Twice-refocused spin-echo (TRSE) sequences [42] can be more economic than PGSE and produce less eddy-current distortions. Clayden [43] demonstrates optimization of TRSE protocols, but using only rectangular gradient waveforms. Extension of our waveform optimization procedure potentially extends to more complex pulse sequence structures, although waveform representations that enforce necessary constraints, such as $\int g(t)\mathrm{d}t = 0$, may be more challenging to find.

We also fix the orientation of the gradient throughout. The algorithm extends naturally to allow the gradient orientation to vary during the waveform. Such variation may provide additional sensitivity to pore size [23,44–46,39,47].

The optimization framework adapts easily to other models of diffusion. Here we fix the axon radius a and the axon direction $\mathbf{n}$ to one value. Future work will expand this by introducing integra-

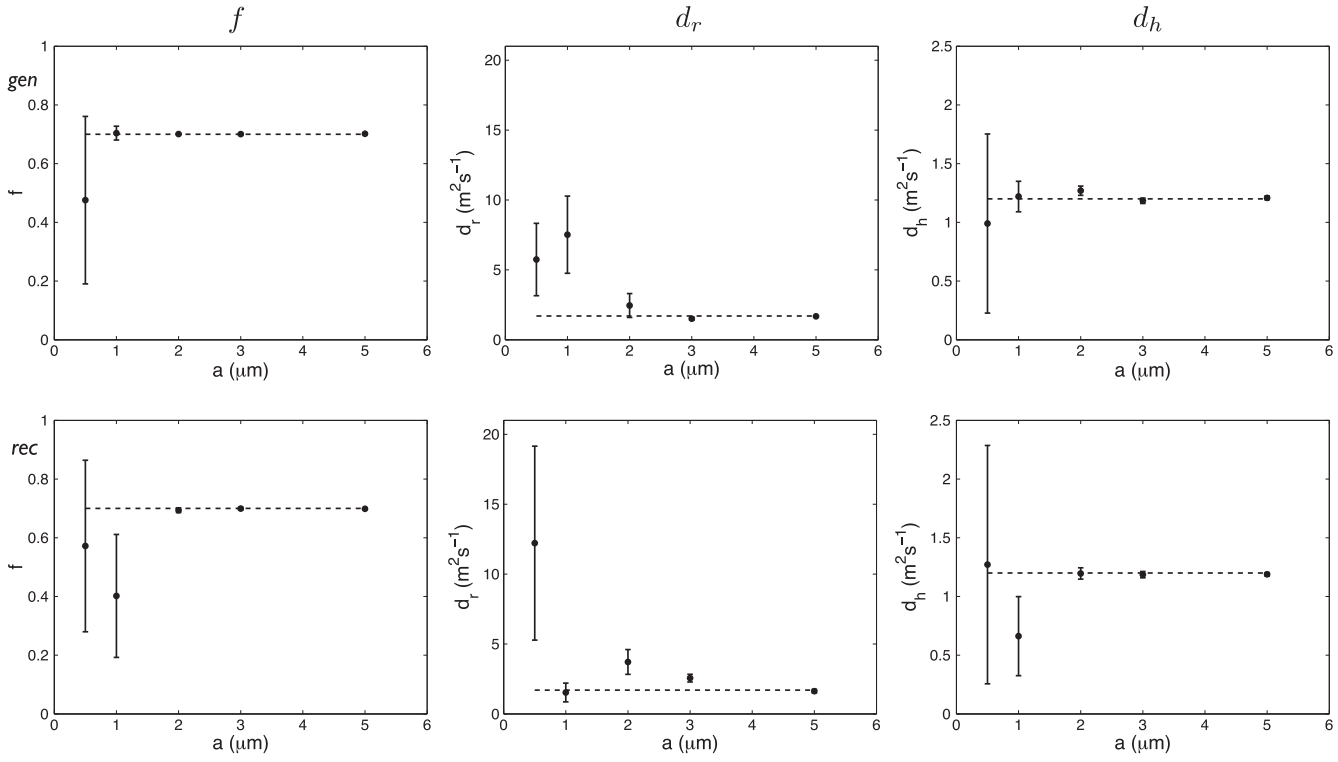

Fig. 10. As Fig. 9 for $G_{max} = 0.08$ T/m.

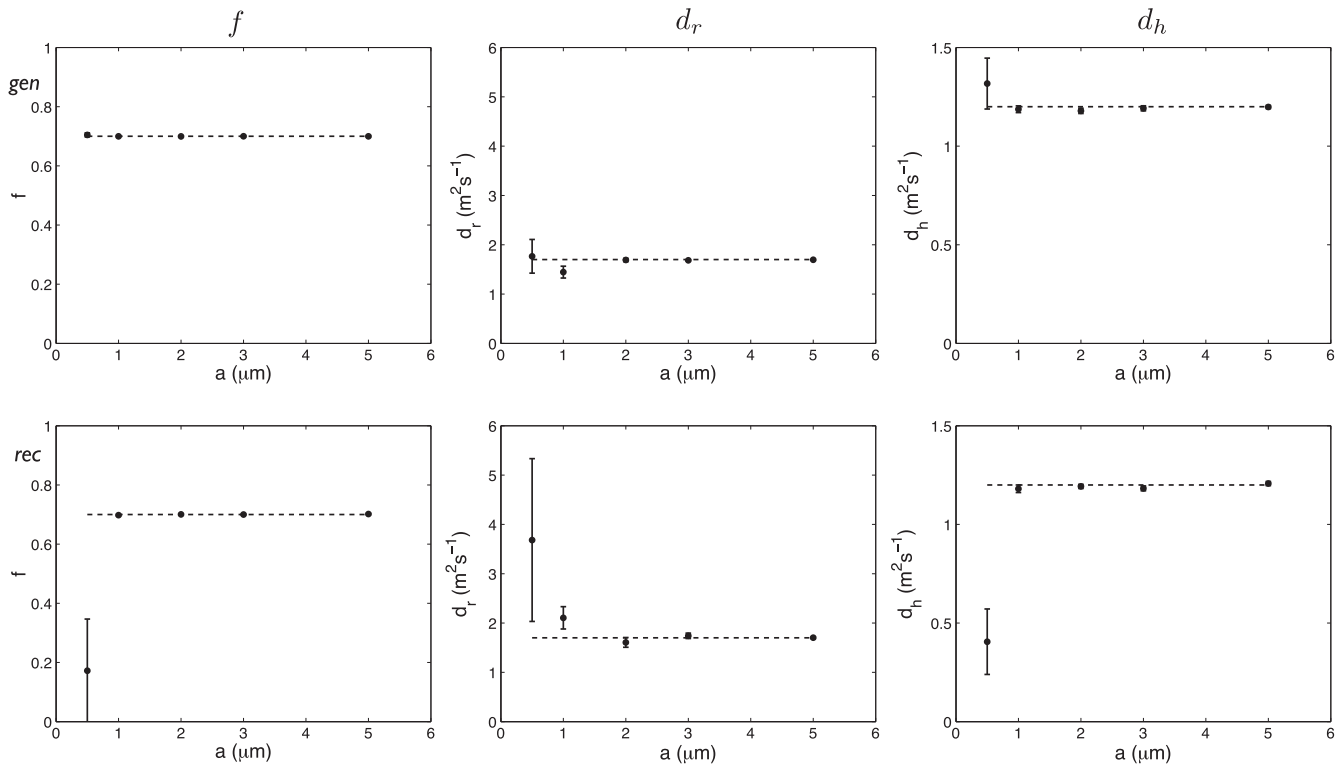

Fig. 11. As Fig. 9 for G_{max} = 0.4 T/m.

tion over a model distribution for *a*, as in [34], to include a distribution of axon radii. Preliminary experiments with this idea show that the optimized protocols for a tissue model with two or three radii, tend to contain the highest frequency waveform measurements from each single-radius protocol. These results suggest that the wider the range of a-priori radii the wider the range of frequencies in the optimized protocol. Furthermore, when the optimized protocol for a particular radii is applied to a tissue model of a different radius, we find that it is significantly better than estimates from the optimized standard PGSE protocols. In applications that estimate indices of a distribution of pore sizes [10,27] therefore, we expect significant improvements moving to optimized general waveform protocols over PGSE, but more incremental further improvement by refining the choice of a-priori radii. Integration over a model distribution for **n** incorporates a distribution of fiber directions. Depending on the application and the parameters of interest, models can for example include: compartment wall permeability which a pair of coupled differential equations [8] can model; additional compartments such as glial cells in the white matter, which a third compartment with spherical restriction might model, as in [8]; varying relaxation times between compartments, as in [48].

The optimized gradient waveforms we presented here can be easily implemented on the real scanner systems since we purposefully constrain the optimization to produce realizable waveforms, and the gradients commonly available on MRI systems can readily oscillate at frequencies of the order of kilohertz [11]. Complicated waveforms with very high frequencies can potentially create difficulties due to artifacts such as eddy-currents or gradient heating. Practical implementation will need to handle any such problems. However, extra constraints are straightforward to include in the optimization, and these can be implemented to minimize the artifacts.

Other factors of in vivo experiments might influence the extraction of parameters. In order to simulate noise we use SNR = 20 here, which we believe is a reasonable for in vivo experiments. Additional experiments (not shown) verify consistent improvement with the optimized generalized waveforms over the optimized rectangular waveforms for a range of SNR. We do not consider further possible complications from movement and physiological noise. However, recent work [10,27] manages to overcome these problems when using PGSE protocols. These factors should present no greater challenge for an optimized waveform measurements.

Previous work [11,28] studies an oscillating gradient method for measuring pore sizes and compare various kinds of oscillation. Our aims are quite different: we look for the best possible waveform shape for a given application, e.g. for estimation of the axon radius, with no prior assumptions about its form except to satisfy the hardware constraints. We are not limited to oscillations, although the optimal shapes do contain oscillations. Callaghan and Stepisnik [29,30] theoretically determine that oscillating waveforms have optimal properties in general for measuring spin motion. Here, we take a more empirical approach and optimize not only one waveform but the whole imaging protocol, which can contain many different measurements, for a specific model. The proposed optimization framework, in which the waveforms and other imaging parameters are learned, is a very novel approach to pulse-sequence and image protocol design that extends to a wide range of imaging applications.

References

[1] P.T. Callaghan, A. Coy, T.P.J. Halpin, D. MacGowan, K.J. Packer, F.O. Zelaya, Diffusion in porous systems and the influence of pore morphology in pulsed gradient spin-echo nuclear magnetic resonance studies, J. Chem. Phys. 97 (1992) 651.
[2] A. Coy, P.T. Callaghan, Pulsed gradient spin-echo NMR "diffusive diffraction" experiments on water surrounding close-packed polymer spheres, J. Colloid Interface Sci. 168 (2) (1994) 373–379.
[3] P.T. Callaghan, K.W. Jolley, J. Lelievre, Diffusion of water in the endosperm tissue of wheat grains as studied by pulsed field gradient nuclear magnetic resonance, Biophys. J. 28 (1) (1979) 133–141.
[4] S. Godefroy, P. Callaghan, 2D relaxation/diffusion correlations in porous media, Magn. Reson. Imaging 21 (3–4) (2003) 381–383.

[5] N.L. Zakhartchenko, V.D. Skirda, R.R. Valiullin, Self-diffusion of water and oil in peanuts investigated by PFG NMR, Magn. Reson. Imaging 16 (5–6) (1998) 583–586.
[6] S. Umbach, E. Davis, J. Gordon, P. Callaghan, Water self-diffusion coefficients and dielectric properties determined for starch–gluten–water mixtures heated by microwave and by conventional methods, Cereal Chem. 69 (6) (1992) 637–642.
[7] P.T. Callaghan, C.D. Eccles, Y. Xia, NMR microscopy of dynamic displacements: k-space and q-space imaging, J. Phys. E: Sci. Instrum. 21 (1988) 820.
[8] G.J. Stanisz, A. Szafer, G.A. Wright, R.M. Henkelman, An analytical model of restricted diffusion in bovine optic nerve, Magn. Reson. Med. 37 (1) (1997) 103–111.
[9] Y. Assaf, T. Blumenfeld-Katzir, Y. Yovel, P.J. Basser, AxCaliber: a method for measuring axon diameter distribution from diffusion MRI, Magn. Reson. Med. 59 (6) (2008) 1347–1354.
[10] D. Barazany, P. Basser, Y. Assaf, In vivo measurement of axon diameter distribution in the corpus callosum of rat brain, Brain 132 (5) (2009) 1210.
[11] J. Xu, M. Does, J. Gore, Sensitivity of MR diffusion measurements to variations in intracellular structure: effects of nuclear size, Magn. Reson. Med. 61 (2009) 828–833.
[12] J.B. Hursh, Conduction velocity and diameter of nerve fibers, Am. J. Physiol. 127 (13) (1939) 1–139.
[13] J.M. Ritchie, On the relation between fibre diameter and conduction velocity in myelinated nerve fibres, Proc. R. Soc. London, B 217 (1206) (1982) 29–35.
[14] J. Piven, J. Bailey, B.J. Ranson, S. Arndt, An MRI study of the corpus callosum in autism, Am. J. Psychiatry 154 (8) (1997) 1051.
[15] J.R. Hughes, Autism: the first firm finding = underconnectivity?, Epilepsy Behav 11 (1) (2007) 20–24.
[16] S. Cluskey, D.B. Ramsden, Mechanisms of neurodegeneration in amyotrophic lateral sclerosis, Mol. Pathol. 54 (6) (2001) 386.
[17] T. Heads, M. Pollock, A. Robertson, W.H.F. Sutherland, S. Allpress, Sensory nerve pathology in amyotrophic lateral sclerosis, Acta Neuropathol. 82 (4) (1991) 316–320.
[18] P.L. Randall, Schizophrenia, abnormal connection, and brain evolution, Med. Hypotheses 10 (3) (1983) 247–280.
[19] D. Rice, S.B. Jr, Critical periods of vulnerability for the developing nervous system: evidence from humans and animal models, Environ. Health Perspect. 108 (Suppl. 3) (2000) 511.
[20] D. Zink, A.H. Fischer, J.A. Nickerson, Nuclear structure in cancer cells, Nat. Rev. Cancer 4 (9) (2004) 677–687.
[21] D. Alexander, A general framework for experiment design in diffusion MRI and its application in measuring direct tissue-microstructure features, Magn. Reson. Med. 60 (2) (2008) 439–448.
[22] P.T. Callaghan, A. Coy, D. MacGowan, K.J. Packer, F.O. Zelaya, Diffraction-like effects in NMR diffusion studies of fluids in porous solids, Nature 351 (1991) 467–469.
[23] L. Avram, Y. Assaf, Y. Cohen, The effect of rotational angle and experimental parameters on the diffraction patterns and micro-structural information obtained from q-space diffusion NMR: implication for diffusion in white matter fibers, J. Magn. Reson. 169 (1) (2004) 30–38.
[24] D. Topgaard, O. Söderman, Experimental determination of pore shape and size using q-space NMR microscopy in the long diffusion-time limit, Magn. Reson. Imaging 21 (1) (2003) 69–76.
[25] H.H. Ong, A.C. Wright, S.L. Wehrli, A. Souza, E.D. Schwartz, P.K. Saha, F.W. Wehrli, Q-space propagator maps of mouse spinal cord provide insight into regional axonal architecture, Proc. Intl. Soc. Mag. Reson. Med. 14 (2006) 640.
[26] J. Latt, M. Nilsson, C. Malmborg, H. Rosquist, R. Wirestam, F. Stahlberg, D. Topgaard, S. Brockstedt, Accuracy of q-space related parameters in MRI: simulations and phantom measurements, IEEE Trans. Med. Imaging 26 (11) (2007) 1437.
[27] D. Alexander, P.L. Hubbard, M.G. Hall, E.A. Moore, M. Ptito, G.J. Parker, T.B. Dyrby, Orientationally invariant indices of axon diameter and density from diffusion MRI, NeuroImage, 2010, doi:10.1016/j.neuroimage.2010.05.043.
[28] E.C. Parsons Jr, M.D. Does, J.C. Gore, Temporal diffusion spectroscopy: theory and implementation in restricted systems using oscillating gradients, Magn. Reson. Med. 55 (2006) 75–84.
[29] P.T. Callaghan, J. Stepisnik, Frequency-domain analysis of spin motion using modulated-gradient NMR, J. Magn. Reson., Ser. A 117 (1) (1995) 118–122.
[30] J. Stepisnik, Analysis of NMR self-diffusion measurements by a density matrix calculation, Physica 104B (1981) 350–364.
[31] A. Kiruluta, Probing restrictive diffusion dynamics at short time scales, J. Magn. Reson. 192 (2008) 27–36.
[32] P.T. Callaghan, A simple matrix formalism for spin echo analysis of restricted diffusion under generalized gradient waveforms, J. Magn. Reson. 129 (1) (1997) 74–84.
[33] S.L. Codd, P.T. Callaghan, Spin echo analysis of restricted diffusion under generalized gradient waveforms: planar, cylindrical, and spherical pores with wall relaxivity, J. Magn. Reson. 137 (2) (1999) 358–372.
[34] Y. Assaf, R.Z. Freidlin, G.K. Rohde, P.J. Basser, New modeling and experimental framework to characterize hindered and restricted water diffusion in brain white matter, Magn. Reson. Med. 52 (5) (2004) 965–978.
[35] E.O. Stejskal, J.E. Tanner, Spin diffusion measurements: spin echoes in the presence of a time-dependent field gradient, J. Chem. Phys. 42 (1) (1965) 288.
[36] W.S. Price, Pulsed-field gradient nuclear magnetic resonance as a tool for studying translational diffusion: Part II. Experimental aspects, Concepts Magn. Reson. 10 (4) (1998) 197–237.
[37] I. Zelinka, SOMA-self-organizing migrating algorithm, in: B.V. Babu, G. Onwubolu (Eds.), New Optimization Techniques in Engineering, Springer, 2004.
[38] E. Özarslan, P.J. Basser, MR diffusion – "diffraction" phenomenon in multi-pulse-field-gradient experiments, J. Magn. Reson. 188 (2) (2007) 285–294.
[39] E. Özarslan, P.J. Basser, Microscopic anisotropy revealed by NMR double pulsed field gradient experiments with arbitrary timing parameters, J. Chem. Phys. 128 (2008) 154511.
[40] K.D. Merboldt, W. Hanicke, J. Frahm, Diffusion imaging using stimulated echoes, Magn. Reson. Med. 19 (2) (1991) 233–239.
[41] K.L. Miller, B.A. Hargreaves, G.E. Gold, J.M. Pauly, Steady-state diffusion-weighted imaging of in vivo knee cartilage, Magn. Reson. Med. 51 (2) (2004) 394–398.
[42] T.G. Reese, O. Heid, R.M. Weisskoff, V.J. Wedeen, Reduction of eddy-current-induced distortion in diffusion MRI using a twice-refocused spin echo, Magn. Reson. Med. 49 (1) (2003) 177–182.
[43] J.D. Clayden, Z. Nagy, M.G. Hall, C.A. Clark, D.C. Alexander, Active imaging with dual spin-echo diffusion MRI, in: Proceedings of the 21st International Conference on Information Processing in Medical Imaging, 2009, p. 275.
[44] P.P. Mitra, Multiple wave-vector extensions of the NMR pulsed-field-gradient spin-echo diffusion measurement, Phys. Rev. B 51 (21) (1995) 15074–15078.
[45] M.A. Koch, J. Finsterbusch, Compartment size estimation with double wave vector diffusion-weighted imaging, Magn. Reson. Med. 60 (1) (2008) 90–101.
[46] M.E. Komlosh, M.J. Lizak, F. Horkay, R.Z. Freidlin, P.J. Basser, Observation of microscopic diffusion anisotropy in the spinal cord using double-pulsed gradient spin echo MRI, Magn. Reson. Med. 59 (4) (2008) 803–809.
[47] N. Shemesh, E. Özarslan, P.J. Basser, Y. Cohen, Measuring small compartmental dimensions with low-q angular double-PGSE NMR: the effect of experimental parameters on signal decay, J. Magn. Reson. 198 (1) (2009) 15–23.
[48] B. Hansen, P. Vestergaard-Poulsen, Mapping the parameter space of a T2-dependent model of water diffusion MR in brain tissue, Magn. Reson. Imaging 24 (8) (2006) 1031–1038.